Direct observations of NO_x emissions over the San Joaquin Valley using airborne flux measurements during RECAP-CA 2021 field campaign

Qindan Zhu[1,*], Bryan Place[2,**], Eva Y. Pfannerstill[3], Sha Tong[4,5], Huanxin Zhang[4], Jun Wang[4], Clara M. Nussbaumer[1,6], Paul Wooldridge[2], Benjamin C. Schulze[7], Caleb Arata[8], Anthony Bucholtz[9], John H. Seinfeld[7], Allen H. Goldstein[3,8], and Ronald C. Cohen[1,2]

[1]Department of Earth and Planetary Sciences, University of California, Berkeley, Berkeley, CA 94720, United States
[*]Now at Department of Earth, Atmospheric and Planetary Sciences, Massachusetts Institute of Technology, Cambridge, MA, United States of America
[2]Department of Chemistry, University of California, Berkeley, Berkeley, CA 94720, United States
[**]Now at Office of Research and Development, U.S. Environmental Protection Agency, Research Triangle Park, North Carolina 27711, United States
[3]Department of Environmental Science, Policy, and Management, University of California, Berkeley, Berkeley, CA 94720, United States
[4]Department of Chemical and Biochemical Engineering, Center for Global and Regional Environmental Research, and Iowa Technology Institute, University of Iowa, Iowa City, Iowa 52242, United States
[5]Collaborative Innovation Center on Forecast and Evaluation of Meteorological Disasters (CIC-FEMD), Key Laboratory for Aerosol-Cloud-Precipitation of China Meteorological Administration, Nanjing University of Information Science Technology, Nanjing 210044, People's Republic of China
[6]Department of Atmospheric Chemistry, Max Planck Institute for Chemistry, Mainz 55128, Germany
[7]Department of Environmental Science and Engineering, California Institute of Technology, Pasadena, CA 91125, United States
[8]Department of Civil and Environmental Engineering, University of California, Berkeley, Berkeley, CA 94720, United States
[9]Department of Meteorology, Naval Postgraduate School, Monterey, CA 93943, United States

Correspondence: Qindan Zhu (qindan_zhu@berkeley.edu) and Ronald C. Cohen (rccohen@berkeley.edu)

Abstract. Nitrogen oxides (NO_x) are principle components of air pollution and serve as important ozone precursors. As the San Joaquin Valley (SJV) experiences some of the worst air quality in the United States, reducing NO_x emissions is a pressing need, yet quantifying current emissions is complicated due to a mixture of mobile and agriculture sources. We performed airborne eddy covariance flux measurements during the Re-Evaluating the Chemistry of Air Pollutants in CAlifornia (RECAP-CA) field campaign in June 2021. Combining footprint calculations and land cover statistics, we disaggregate the observed fluxes into component fluxes characterized by three different land cover types. On average we find emissions of 2.95 mg m^{-2} h^{-1} over highways, 1.24 mg m^{-2} h^{-1} over urban areas and 0.79 mg m^{-2} h^{-1} over croplands. The calculated NO_x emissions using flux observations are utilized to evaluate anthropogenic emission inventories and soil NO_x emission schemes. We show that two anthropogenic inventories for mobile sources, EMFAC (EMssion FACtor) and FIVE (Fuel-based Inventory for Vehicle Emissions), yield similar agreement with emissions derived from measured fluxes over urban regions with 24% and 22% low bias, respectively. Three soil NO_x schemes, including MEGAN v3 (Model of Emissions of Gases and Aerosols from Nature), BEIS v3.14 (Biogenic Emission Inventory System) and BDISNP (Berkeley Dalhousie Iowa Soil NO Parameterization), show

substantial underestimates over the study domain. Compared to the cultivated soil NO_x emissions derived from measured fluxes, MEGAN and BEIS are lower by more than one order of magnitude and BDISNP is lower by a factor of 2.7. Despite
15   the low bias, observed soil NO_x emissions and BDISNP present a similar spatial pattern as well as temperature dependence. We conclude that soil NO_x is a key feature of the NO_x emissions in the SJV and that a state-of-the-science model of these emissions is needed to simulate emissions for modeling air quality in the region.

1   Introduction

Nitrogen oxides ($NO_x \equiv NO + NO_2$) are important trace gases that affect both the gas and aerosol phases of tropospheric
20   chemistry. NO_x regulates the concentrations of the primary atmospheric oxidant, hydroxyl radicals (OH), and serves as the catalyst for the formation of ozone (O_3). NO_x also affects the formation of inorganic nitrate aerosol through the production of nitric acid (HNO_3) and organic nitrates ($RONO_2$) and plays a role in secondary organic aerosol (SOA) production. NO_x, O_3 and aerosol are all detrimental to human health, triggering respiratory diseases (Kampa and Castanas, 2008; Hakeem et al., 2016) and leading to premature death (Lelieveld et al., 2015).
25   NO_x is predominantly emitted from anthropogenic sources, including light and heavy-duty transportation, fuel combustion, and biomass burning. Among these sectors transportation is the largest in the United States (EPA, 2016). Strict regulations have been implemented to control NO_x emissions. Three-way catalysts have effectively reduced emissions from gasoline-powered passenger vehicles. The application of emission control systems on coal power plants has reduced NO_x emissions (De Gouw et al., 2014). The California Air Resources Board (CARB) has proposed Heavy-Duty Engine and Vehicle Omnibus
30   Regulation and Associated Amendments and target for 90% reduction in per-vehicle heavy-duty NO_x emission by 2031(CARB, 2016). The regulation of mobile sources leads to an increasing importance of natural NO_x sources, such as lightning and soil emissions. Soil NO_x is released as a byproduct of microbial nitrification and denitrification (Andreae and Schimel, 1990). While the biogeochemistry of soil NO_x emission is well established, this biogenic source involves a complex interaction of soil microbial activity, soil nitrogen (N) content. Besides, agriculture activities, such as the use of fertilizers, lead to a substantial
35   enhancement of soil NO_x emissions (Phoenix et al., 2006).
Currently, the San Joaquin Valley (SJV) in California experiences some of the most severe air pollution in the United States. The SJV cities, Visalia, Fresno, and Bakersfield are among the top ten most polluted cities for both ozone and particulate matter (American Lung Association, 2020). In order to implement appropriate emission control efforts, identifying the contribution of different NO_x emissions are particularly important for the SJV as it features a complex mixture of emissions from fuel
40   combustion and soil emissions associated with agriculture. Almaraz et al. (2018) argued that due to growing N fertilizer use, the SJV has soil NO_x emissions of 24 kg of N ha^{-1} year^{-1}, contributing 20-51% of the NO_x budget of the entire state of California. In contrast, Guo et al. (2020) attribute approximately 1.1% of anthropogenic NO_x emissions in California to soil NO_x.
Airborne eddy covariance (EC) flux measurements provide a powerful tool to investigate the emission strength of atmo-
45   spheric constituents at landscape scales. It has been applied to assess the surface exchanges of greenhouse houses (GHGs)

including CO_2 and methane (CH4) (Mauder et al., 2007; Yuan et al., 2015; Sayres et al., 2017; Hannun et al., 2020). In recent years it has been extended to study emissions of volatile organic compounds and NO_x over a megacity (Karl et al., 2009; Vaughan et al., 2021), vegetation (Karl et al., 2013; Misztal et al., 2014; Wolfe et al., 2015; Kaser et al., 2015; Yu et al., 2017; Gu et al., 2017), and shale gas production regions (Yuan et al., 2015). Compared to the traditional EC measurements from in-
50 struments mounted at a fixed location on a tower, wavelet-based airborne EC measurements allow for larger spatial assessment and are well suited to regions with inhomogeneous and non-stationary source distributions (Sühring et al., 2019).

In this study, we present airborne EC flux measurements obtained during seven flights of a Twin Otter aircraft over the San Joaquin Valley in California. Companion studies of NO_x emissions over Los Angeles (Nussbaumer et al. 2022, submitted) and VOC (Pfannerstill et al. in prep) and GHG fluxes (Schulze et al. in prep) will be presented separately. We utilize continuous
55 wavelet transformation to calculate the NO_x flux (Sect. 3). In conjunction with footprint calculations and land classification, we explore the spatial heterogeneity of NO_x emissions and identify component fluxes from the highway, urban and soil land types (Sect. 4). We also utilize the NO_x emissions derived from flux measurements to evaluate anthropogenic emission inventories and soil NO_x schemes (Sect. 5).

2 Measurements

60 The airborne EC flux measurements were conducted on a Twin Otter research aircraft operated by the Naval Postgraduate School (NPS) during the Re-Evaluating the Chemistry of Air Pollutants in CAlifornia (RECAP-CA) field campaign. The RECAP-CA field campaign was conducted between June 1st to June 22nd in California, including 7 days of measurements over the San Joaquin Valley and 9 days of measurements over Los Angeles. The flight path was designed with long straight legs to ensure good quality of flux measurements (Figure S1) (Karl et al., 2013). The aircraft flew slowly, at the airspeed of
65 50-60 m/s, and cruised at a low height of ~ 300 m above ground. The aircraft took off at $\sim$11:00 local time at Burbank Airport and landed at $\sim$18:00 local time.

The standard instruments aboard the aircraft are described in (Karl et al., 2013) and include total and dew point temperature, barometric and dynamic pressures, wind direction and wind speed, total airspeed, slip- and attack angles, GPS latitude, GPS longitude, GPS altitude, pitch, roll and heading. These measurements are at 10Hz temporal resolution.
70 Mixing ratios of NO_x were measured at 5 Hz frequency using a three-channel custom-built thermal dissociation-laser induced fluorescence (TD-LIF) instrument. Ambient air was sampled at a rate of $\sim$6 L/min and the sample flow was split equally between the three instrument channels. The first channel provided measurements of NO_2 via the laser-induced fluorescence of NO_2 molecules with a compact green laser (Spectra-Physics ExplorerOneXP 532 nm). The laser was pulsed at 80 kHz and the 1.7 Watt average power was split between the three cells. An excess flow of O_3 was introduced into the second channel to
75 provide measurements of total NO_x by converting all NO in the sample flow to NO_2 before detection. The red-shifted fluorescence from the NO_2 molecules was collected, wavelength filtered and quantified with time gated photon counting modules (Hamamatsu H7421-50). The third TD-LIF channel was used to measure the sum of all other higher nitrogen oxides (NO_z) by thermally dissociating NO_z to NO_2 with an inline oven ($\sim$500 C) before LIF detection. All three detection cells were

maintained at low pressure ($\sim$0.4 kPa) to minimize collisional quenching of the NO_2 molecules and to extend the fluorescence

80 lifetime so the observing gate can be limited to the time after the laser pulse. Instrument calibrations were performed in-flight every 60 minutes using a standardized NO_2 cylinder (Praxair, 5.5 ppm, Certified Standard grade) diluted with scrubbed air. In addition, instrument zeros were run using ambient air scrubbed of all reactive gases every 20 minutes in flight to correct for any background drift during the flights. A more complete description of the TD-LIF instrument specifics and analytical performance can be found in previous literature (Thornton et al., 2000; Day et al., 2002; Wooldridge et al., 2010)

85 **3   Flux and footprint calculation**

3.1   Pre-processing

The observed 10 Hz vertical wind speeds are downscaled to 5 Hz in order to match the time resolution of NO_x measurements. The full observation data set breaks into segments with continuous wind and NO_x measurements. The segment window is selected if the length is larger than 10 km and the height variation is less than 200 m. We also filter out measurements when

90 aircraft roll angles are larger than 8 degrees to avoid perturbation in the vertical wind due to aircraft activity. While most of the measurements are within the boundary layer, the airplane arose above the boundary layer occasionally. We obtain the hourly boundary layer height from the High-Resolution Rapid Refresh (HRRR) product at the spatial resolution of 3 km. The observations are removed if the aircraft exceeds the planetary boundary layer (PBL) height from HRRR.

We adjust for the lag time between the meteorology measurements and the TD-LIF measurements by shifting the time of

95 TD-LIF observation within the time window of $\pm$ 4 seconds until the covariance with the vertical wind speed is maximized (Figure. S4). As the time lag is assumed to be due to differences in the clocks of the two instruments and the transit time of air through the TD-LIF instrument, we assume that the lag time for each flight is constant. We use the median lag time from each flight for all segments collected on the same day.

3.2   Continuous wavelet transformation

100 The continuous wavelet transformation (CWT) parameterization decomposes the time series ($x(t)$) into a range of frequencies and represents it as the convolution of the time series with a wavelet function.

$$W(a,b) = \int_{\infty}^{-\infty} x(t)\psi^*_{a,b}(t)dt \tag{1}$$

$$\psi^*_{a,b}(t) = \frac{1}{\sqrt{a}}\psi_0(\frac{t-b}{a}) \tag{2}$$

where $W(a,b)$ is the wavelet coefficient; $\psi^*_{a,b}(t)$ is the wavelet function, which is based on a "mother" wavelet ψ_0 and is

105 adjusted with a transition parameter b and a scale parameter a. The transition parameter determines the location of the "mother" wavelet and the scale parameter defines the frequency. We use the Morlet wavelet as the "mother" wavelet.

$$\psi_0 = \pi^{-1/4}e^{6i\eta}e^{-\eta^2/2} \tag{3}$$

The Morlet wavelet has been widely applied to represent turbulence in the atmosphere due to a reasonable localization in the frequency domain and a good ability of edge detection (Schaller et al., 2017).

110   Time domain scales are increased linearly with the increment of the time resolution (δt, $0.2s$), and frequency domain scales are represented by an exponential array of scale parameters a_j with the increment δj of $0.25s$. The largest frequency scale is the Nyquist frequency, which is twice the time resolution ($0.4s$).

$$b_n = n\delta t \tag{4}$$

$$a_j = a_0 \times 2^{j\delta j} \tag{5}$$

115   For two simultaneous time series of NO_x ($W_c(a,b)$) and vertical wind speed ($W_w(a,b)$), we obtain the wavelet cross-spectrum (Eqn. 6). The Morlet wavelet-specific reconstruction factor C_δ is 0.776. We then sum up over the full frequency scales to yield a time series of flux (Eqn. 7).

$$E_{c,w}(j) = \frac{\delta t}{C_\delta} \frac{1}{N} \sum_{n=0}^{N-1} [W_c(a,b) \cdot W_w^*(a,b)] \tag{6}$$

$$F(t) = \overline{c'w'} = \frac{\delta t}{C_\delta} \frac{\delta j}{N} \sum_{n=0}^{N-1} \sum_{j=0}^{J} \frac{[W_c(a,b) \cdot W_w^*(a,b)]}{a(j)} \tag{7}$$

120   Figure 1 exhibits an example of CWT flux calculation. Figure 1 (a) shows the detrended NO_x and vertical wind speed in a straight segment of ~ 50 km. The detrending is realized by subtracting out the average followed by dividing the standard deviation of a scalar time series. Both time series are decomposed using CWT algorithm to yield the cross-power spectrum shown in Figure 1 (b). Due to the finite length in time, the wavelet power spectrum is prone to higher uncertainties closer to the edge (Mauder et al., 2007). The regions of the wavelet power spectrum where the edge effects are the largest are identified as
125   the Cone of Influence (COI). Data points containing >80% spectral power within the cone of influence are removed for quality control. The power spectrum is then integrated over all frequencies to the time series of NO_x flux (Figure 1 (c)). To address the influence of large-scale turbulence, we processed the integrated fluxes as 2 km moving averages and re-sampled them at 500 m.

3.3   Footprint calculation

130   The footprint describes the contribution of surface regions to the observed airborne flux. We use the KL04-2D parameterization to calculate a space-resolved footprint map. This KL04-2D parameterization is developed from a 1-D backward Lagrangian stochastic particle dispersion model (Kljun et al., 2004). Metzger et al. (2012) implemented a Gaussian cross-wind distribution function to resolve the dispersion perpendicular to the main wind direction. The input parameters include the height of the measurements, standard deviation of horizontal and vertical wind speed, horizontal wind direction, boundary layer height,
135   surface roughness length, and friction velocity. We obtain the boundary layer height and surface roughness length from the HRRR product. The friction velocity is inferred using the logarithmic wind profile given the observed horizontal wind speed, measurement height, and surface roughness length (Högström, 1988).
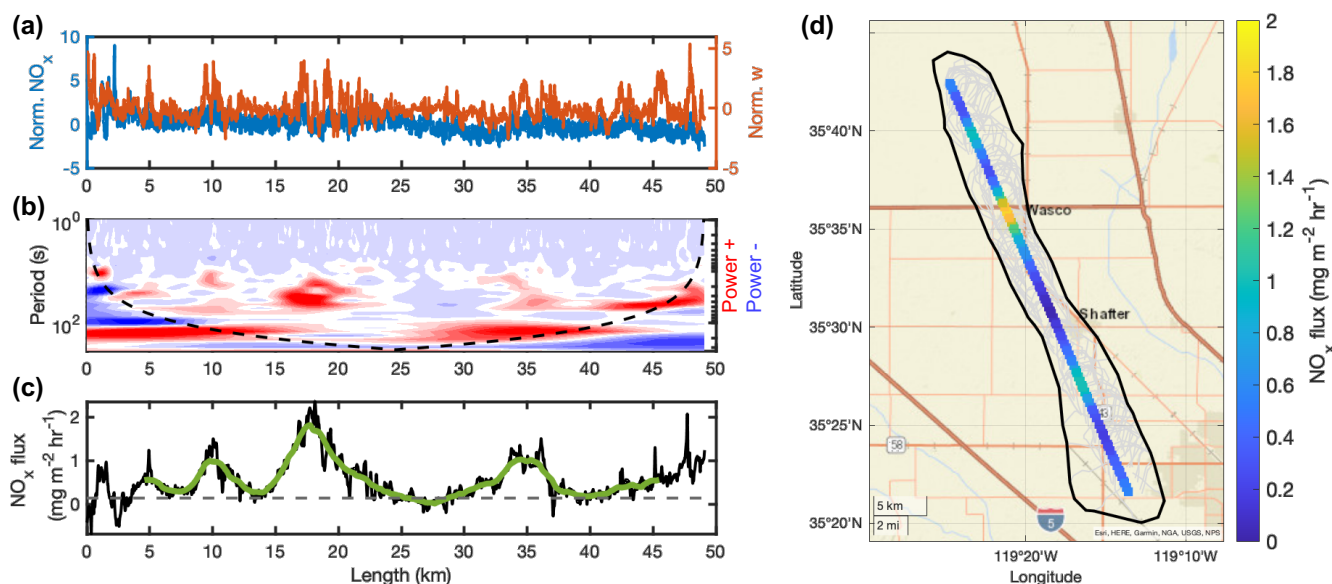
Figure 1. a) The variance of NO_x and vertical wind speed, b) frequency and time-resolved wavelet power spectrum with the cone of influence shown as a black dotted line, c) the integrated fluxes from the raw data points are shown in black, the fluxes after moving averaging and COI filtering are shown in green. The dashed gray line indicates the detection limit of this segment. d) the distribution map of flux re-sampled at 500m. The gray lines show the 9th percentiles of the footprints and the black line denotes the contours of all footprints.

Figure 1 (d) depicts the 90% KL04-2D footprint contours of observations resampled to 500 m in one segment. Each footprint contour is aligned with the horizontal wind direction and is transformed into a geographic coordinate space.

140 **3.4 Vertical divergence**

Extrapolating the airborne flux to surface flux should account for the vertical divergence. The vertical divergence is a result of multiple processes, including net in-situ production or loss, storage, and horizontal advection.

To investigate the impact of vertical divergence, the flight route includes three vertically stacked racetracks, during which the segments are close to each other in space but vary in height. After removing the legs that fail the quality control, only one 145 racetrack measurement carried out between 14:20 to 15:10 on June 8th presented qualified flux segments, and the vertical distribution of fluxes is shown in Fig. S4. No consistent increase or decrease of fluxes with increasing height is detected during the racetrack in this study because the vertical divergence is hampered by emission heterogeneity. Shown in Fig. S5, the footprint map for each segment at various altitudes covers regions with high heterogeneity. Therefore, we use an alternative approach to calculate the vertical divergence. Instead of extracting racetrack measurements, we collect a subset of flux measurements 150 during the whole field campaign based on the footprint coverage. Only fluxes with footprints covering croplands exclusively are included to avoid emission heterogeneity. We use PBL height (z_i) from HRRR to calculate the ratio of measurement heights relative to the PBL height (z/z_i). 98% of selected fluxes are located within 70% of the PBL height and they are divided into 7
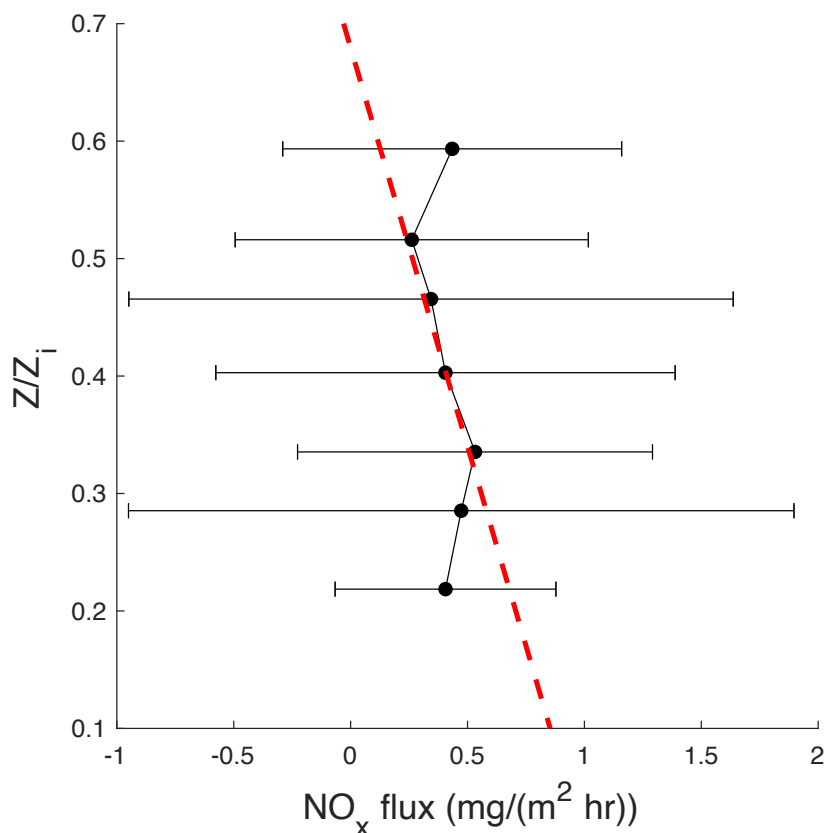
Figure 2. Vertical profiles of measured fluxes above croplands during RECAP-CA field campaign binned by the ratio of measurement height and PBL height (z/z_i). The points represent the median flux within each bin, and the error bars represent the standard deviation. The red dashed line shows a linear fit for median fluxes versus relative height.

bins of z/z_i with uniform width. We then perform a linear fit for the binned median fluxes versus z/z_i and use the regression result to calculate the linearly extrapolated surface fluxes. After vertical divergence correction, the surface fluxes are on average

155 30% higher than the fluxes at the measurement heights.

3.5 Uncertainty analysis

The flux calculation using CWT introduces uncertainty from a variety of sources. We describe systematic errors and random errors following Wolfe et al. (2018).

Systematic errors arise from the under-sampling of high-frequency and low-frequency ranges. The CWT algorithm fails to
160 resolve a frequency higher than the Nyquist frequency. Due to the high temporal resolution of data points (5 Hz), we expect a minimal loss of high-frequency limit (Figure. S3). The upper limit of systematic error associated with low frequency is

calculated using Eqn. 8 (Lenschow et al., 1994).

$$SE \leq 2.2(\frac{z}{z_i})^{0.5}\frac{z_i}{L} \tag{8}$$

z and L are the measurement heights and the length of segments, respectively. z_i are the boundary layer heights from HRRR.
165 We calculate the low-frequency error ranges from 1%-5%.

Random errors define the detection limit of the CWT. The detection limit is assessed by assigning a randomly generated wind speed of a unity standard deviation and recalculating flux using this random wind speed series and observed NO_x mixing ratio. The fractional uncertainty is determined by using $3\times$ standard deviation of the detection limit divided by the average flux for each segment, yielding a mean fractional error of 52% after averaging to 2 km.

170 Estimating the uncertainty caused by the correction of vertical divergence is tricky. While we conclude that the influence of vertical divergence is non-negligible, it is ignored in some previous airborne flux studies (e.g. Vaughan et al., 2016; Hannun et al., 2020; Vaughan et al., 2021; Drysdale et al., 2022). Here we only consider the uncertainty of 20% associated with the linear regression results in the vertical divergence correction. However, the uncertainty is arguably higher and is yet challenging to quantify as we see a significant difference in vertical correction factor on racetrack measurements versus a selected subset 175 of flux observations.

We treat each uncertainty component as independent and calculate the interquartile of total uncertainty to be 40% and 78%. The random error in the CWT algorithm dominates the uncertainty and is consistent with previous studies (Wolfe et al., 2018; Vaughan et al., 2016).

4 Component flux disaggregation

180 The overview of observed fluxes across 7 flights over San Joaquin Valley is illustrated in Fig. 3. It shows a distinct spatial heterogeneity (Figure 3 (a)). For instance, high NO_x flux signals are detected when the aircraft was flying above highway 99 between Bakersfield and Visalia. The transect of cities, such as Fresno, capture a substantial enhancement of NO_x fluxes. Figure 3 (b) exhibits the count density of airborne fluxes. 88% of the fluxes are positive, demonstrating that our airborne flux measurements are capable of detecting NO_x emissions over the study domain. We attribute the remaining 12% of negative 185 fluxes to the uncertainties in calculation including an incomplete sampling of the full spectrum of eddies. The distribution of observed fluxes is right-skewed; the mean and median observed flux over the SJV is 1.01 mg m^{-2} h^{-1} and 0.65 mg m^{-2} h^{-1}, respectively. The interquantile range of flux is 0.27 mg m^{-2} h^{-1} and 1.38 mg m^{-2} h^{-1}. 0.6% of extremely high fluxes exceeding 8 mg m^{-2} h^{-1} represents the long tail in the flux distribution, which are, like the negative fluxes, most likely caused by the incomplete sampling of the spectrum of eddies driving the fluxes.

190 As discussed in Sect. 3.3, we then calculate the footprint for each flux observation during the RECAP field campaign. Figure 3 (a) shows the 90% footprint extent in grey. Fig. S6 shows that the 90% extent for the calculated footprints ranges from 0.25 to 11.7 km with a mean extent of 2.6 km. The KL04-2D footprint algorithm has been applied to airborne flux analysis over London and in that study, the 90% footprint extents range from 3 km to 12 km from the measurement (Vaughan et al., 2021).

While the largest footprint extent is comparable with those from Vaughan et al. (2021), our calculated footprints mostly have

195   a smaller extent as 70% of the footprint extents are within 3 km of the aircraft flight track. We attribute the small footprints to the stagnant weather conditions and weaker horizontal wind advection compared to London. The mean wind speed is 2.9 m/s for full observation data sets and 2.4 m/s for those data points with footprint extents less than 3 km. The largest footprint extent corresponds to observations at the foothills, due to higher altitude above the ground relative to the boundary layer height and stronger horizontal wind advection.

200   The region covered by the footprints is composed of mixed land cover types. We use the 2018 USDA CropScape database (https://nassgeodata.gmu.edu/CropScape/) to describe the land cover types. The resolution has been degraded from the native 30m resolution to 500m. For each grid, the land cover type is assigned if a land type makes up more than 50% of the 500m grid cell. We generalize a "soil" land cover type if the land cover type is identified as either cropland or grassland. The grids classified as "developed" in CropScape are dominated by anthropogenic activities including transportation and fuel combustion.

205   We overlay the national highway network and categorize the grids containing highways as "highway" land types. The remaining grids are classified as "urban" and they correspond to the area with heavy populations in absence of highways. The distinction between "highway" and "urban" land type is utilized to address on-road mobile sources. 28% of the flux observations include the highway land type in the 90% footprint extent, 15% of the observations include the urban land type and 94% of the observations include cultivated soil land type.

210   To disentangle the flux emanating from different land cover types, we apply the Disaggregation combining Footprint analysis and Multivariate Regression (DFMR) methodology described in Hutjes et al. (2010). The observed fluxes are treated as the weighted sum of component fluxes from each land cover type:

$$F_{obs} = \sum_{k=1}^{3} w_k F_k \qquad (9)$$

where w_k is the fractional area within the 90% footprint contour and F_k are the corresponding component fluxes from high-

215   way, urban, and soil land types, respectively. The multi-linear regression is applied to observations from all flights, consisting of 4749 data points. To better quantify the uncertainty, we bootstrap the data samples and re-calculate the multi-linear regression 100 times. The resulting statistical uncertainty is shown in Fig.4. The highway land type yields the highest flux of 2.95 mg m^{-2} h^{-1} with a standard deviation of 0.14 mg m^{-2} h^{-1}. The areas classified as urban land type exhibit a flux of 1.24 ($\pm$0.10) mg m^{-2} h^{-1}, which is 50% of the highway flux. Most likely the fluxes from highway are even higher than 2.95 mg

220   m^{-2} h^{-1}. Note that the land type map is at 500m spatial scale, the grid classified as highway indeed includes both highway and areas near the highway. If, for example, the highway is only 10% of the true area of the land cover pixel, then the fluxes on the highway could be as much as 10 times larger. The cultivated soil land type flux of 0.79 ($\pm$0.02) mg m^{-2} h^{-1} is large. It is about 1/4 the magnitude of the highway flux and half that of the urban flux. As the total area of soil pixels are much larger than the area of highway or urban pixels, integrated across the SJV, cultivated soil NO$_x$ emissions are a major factor.

(a)   **(b)**
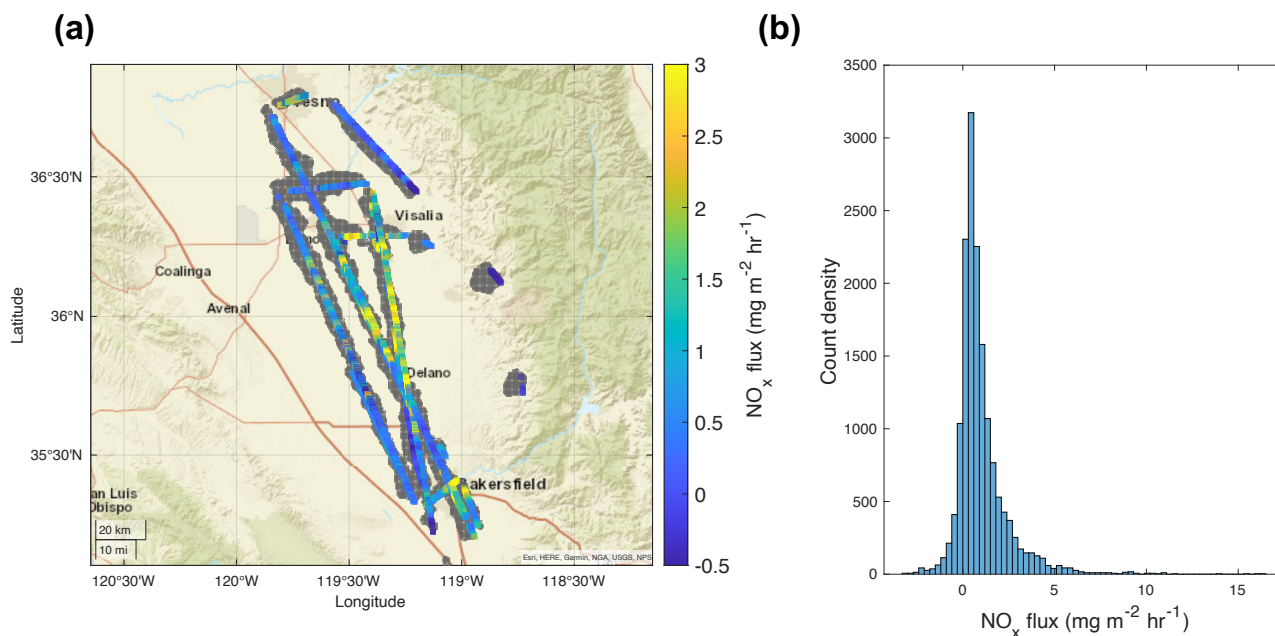
Figure 3. a) The map of observed airborne fluxes over 7 flights over the San Joaquin Valley. If the segment overlaps each other, the average flux is calculated. The grey shade represents the coverage of 90% footprint extents for all flux observations. b) The count density of full data sets of observed airborne fluxes.
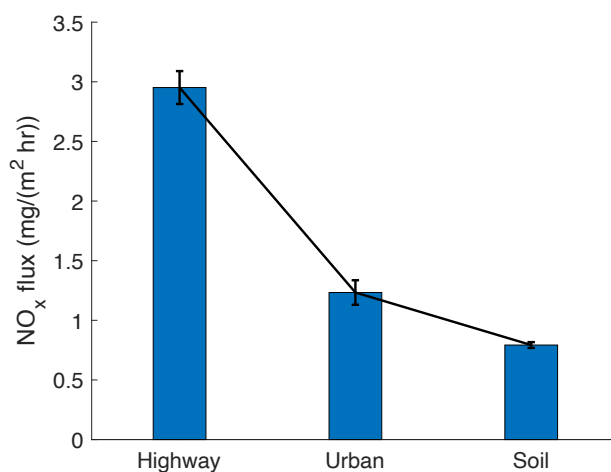
Figure 4. Bootstrapped statistical results of multi-linear regression to resolve component fluxes from the highway, urban, and cultivated soil land types. Each bar represents the average component fluxes from each land type and the black line shows the standard deviation.

5 Calculation of NO_x emission map using airborne NO_x fluxes

While these separate component fluxes emphasize the distinction between individual land types at the spatial resolution of the landscape, the emission map shows the distribution of NO_x fluxes at the spatial resolution of the emission inventory, 4 km. For each 4 km grid, we collect the observed fluxes whose 90% of the footprint overlaps with this grid area and define the weight r_k as the fractional area that the footprint covers. The emission, in a unit of mg m^{-2} h^{-1}, is calculated by the weighted average of flux (Eqn. 10). Only grids measured by at least five flux observations are considered in order to focus our attention on those pixels for which we have a statistically representative sample of the emissions.

$$Emis_i = \frac{\sum_{k=1}^{n \geq 5} r_k F_k}{\sum_{k=1}^{n \geq 5} r_k} \tag{10}$$

The emission is calculated based on the observations from each flight (Fig. 5 (a)). During RECAP-CA, we made six flights during weekdays. The largest reported weekday emission was on June 03 when the median emission was 1.07 mg m^{-2} h^{-1}. The lowest weekday emission was observed on June 15 with the median emission of 0.39 mg m^{-2} h^{-1}. The large daily variation observed in estimated emissions during weekdays is partially due to the variation in flight routes and footprint coverage. This is illustrated by the daily estimated emission map shown in Fig. S7. We also made one weekend flight on June 13, and it yields estimated emissions that are significantly lower than the estimated emission on any weekday, which we attribute to reduced diesel truck activity at the weekend.

As the emission inventories make a distinction between weekdays and weekends and do not account for the daily variation on different weekdays, we average over the six-weekday flights to yield the best estimate of emission maps over the San Joaquin Valley derived from flux measurements (Fig. 5 (b)). The median estimated weekday NO_x emission over the study domain is 0.70 mg m^{-2} h^{-1} with the interquantile range of 0.40 and 1.34 mg m^{-2} h^{-1}. The observed emission map describes high NO_x emissions in the cities of Bakersfield (119°W, 35.3°N) and Fresno (119.8°W, 36.75°N) and along highway 99.

5.1 Evaluation of anthropogenic NO_x emission inventories

First, we compare the observations to the inventory developed by the California Air Resources Board (CARB). The anthropogenic emissions of NO_x consist of mobile sources, stationary sources, and other NO_x emissions from miscellaneous processes such as residential fuel combustion and managed disposal. In the CARB inventory, the mobile sources are estimated from EMission FACtor (EMFAC) v1.0.2 (CARB, 2021a) and OFFROAD mobile source emission models (CARB, 2021b). The stationary sources are estimated based on the reported survey of facilities within each local jurisdiction and the emission factors from California Air Toxics Emission Factor (CATEF) database (CARB, 2021c). Hereinafter we utilize "EMFAC" to represent anthropogenic vehicle-related NO_x emissions used in the CARB inventory. An alternative anthropogenic emission inventory is the fuel-based inventory for vehicle emissions (FIVE), developed by McDonald et al. (2012) and updated by Harkins et al. (2021). Both emission inventories are at 4 km spatial resolution.
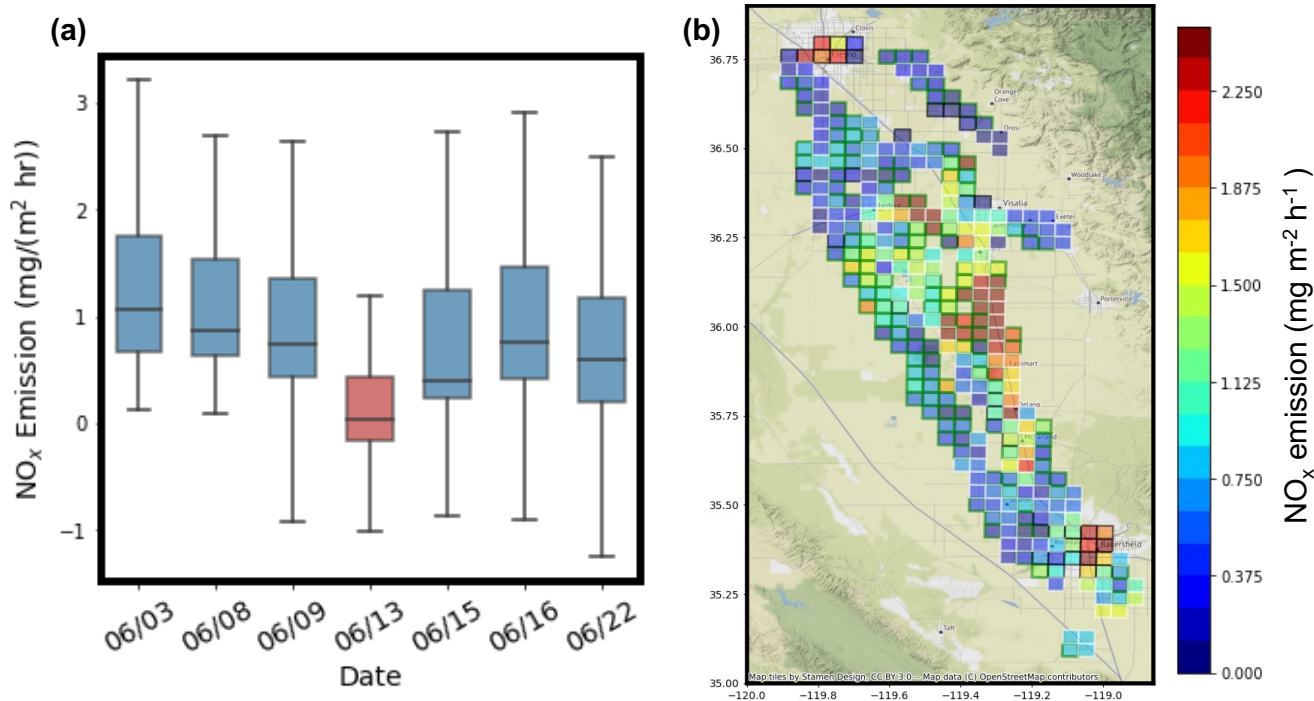
Figure 5. a) The whisker box plot of observed emissions for each flight, aligned in the order of flight days. The box represents the interquartile ranges of observed emissions and the line represents the median emission. The whiskers show the maximum and minimum values. The weekdays are shown in blue and one weekend day is shown in red. b) The spatial distribution of emission at 4 km over SJV derived from observed fluxes during weekdays. The patch color shows the observed NO_x emission. The edge color denotes the land cover type; the grid cells covering highways in white, those covering urban regions in black, and the rest of the grid cells that are categorized with cultivated soil land cover types in green. ©OpenStreetMap contributors 2022. Distributed under the Open Data Commons Open Database License (ODbL) v1.0.

255   To disentangle the contribution of different NO_x emissions sources, we attribute emissions at grid cells covering either highway or urban regions to anthropogenic emissions from transportation and fuel combustion, and those at remaining grid cells are categorized as soil NO_x emissions. For each grid cell categorized as anthropogenic emission dominant, we then match the emission inventories representing the weekday scenario to the same hour and grids of emissions derived from measured fluxes. The corresponding hour of this estimated emission is rounded to the closest hour of the observation times. Figure

260   6 shows the comparison of observed anthropogenic emissions against EMFAC and FIVE emission inventories. Over urban regions, the median observed RECAP NO_x emission is 1.10 mg m^{-2} h^{-1} and the interquartile range is 0.36 and 1.86 mg m^{-2} h^{-1}. Both EMFAC and FIVE yield a good agreement with our measurements; the median urban NO_x emission in these inventories is 24% and 22% lower than the observation, respectively. The estimated NO_x emission on grid cells covering highways is more scattered. The median estimated NO_x emission is 0.68 mg m^{-2} h^{-1}. It is lower than on urban grid cells

265   due to spatial averaging and the fact that most of the highway length is outside the urban regions. The distribution of observed RECAP NO_x emissions from the highway is right-skewed, characterized by an interquartile range of 0.41 and 1.42 mg m^{-2} h^{-1}. We also note that over highway 99, the RECAP NO_x emission is a factor of 3 higher than average on grid cells near congestion, reflecting the variation of emission caused by real-time traffic conditions. Both EMFAC and FIVE provide lower NO_x emissions over highway grids, the median NO_x emissions are 28% and 36% of those from the RECAP observations. The

270   highway pixels include a land cover that is mostly non-highway; typically soil. If soil N emissions are substantially larger than in these inventories, it is possible that the measurements and bottom-up inventories for highways are in better agreement than indicated by the figure.

5.2 Evaluation of soil NO_x scheme

Soil NO_x varies nonlinearly with meteorological conditions, soil conditions, and agricultural activities. The Model of Emis-

275   sions of Gases and Aerosols from Nature v3 (MEGAN) (Guenther et al., 2012) is the most commonly used scheme and is used to predict soil NO_x emissions in the CARB emission inventory. It is gridded at 4 km spatial scale and has hourly time steps. The biogenic Emission Inventory System (BEIS) is the default scheme to estimate volatile organic compounds from vegetation and NO from soil developed by the United States Environmental Protection Agency (EPA). We obtain the hourly BEIS v2.14 soil NO_x emission at 4 km during the study period from the Weather Research and Forecasting-Chemistry model (WRF-Chem)

280   with the same model configuration described in Kim et al. (2022). The Berkeley Dalhousie Iowa Soil NO Parameterization (BDISNP) (Hudman et al., 2012; Sha et al., 2021) is also used in a number of models. This parameterization includes more details than the other two in order to be more faithful to direct measurements made at soils and to describe their seasonal and hourly variations. The BDISNP includes parameters representing the effects of soil moisture, temperature, and soil nitrogen including fertilizer. Using the same WRF-Chem setup described in Sha et al. (2021), we also calculate the BDISNP soil NO_x

285   emissions during the study period at the spatial resolution of 2 km and re-grid them to 4 km.

Figure. 7 (a) illustrates the range of soil N emissions derived from RECAP observations as compared to these three different soil NO_x schemes. The analysis of the observations exhibits a median cultivated soil NO_x emission of 0.68 mg m^{-2} h^{-1} with a wide spread. The interquartile range of the inferred emission is 0.41 mg m^{-2} h^{-1} and 1.22 mg m^{-2} h^{-1}. MEGAN and BEIS
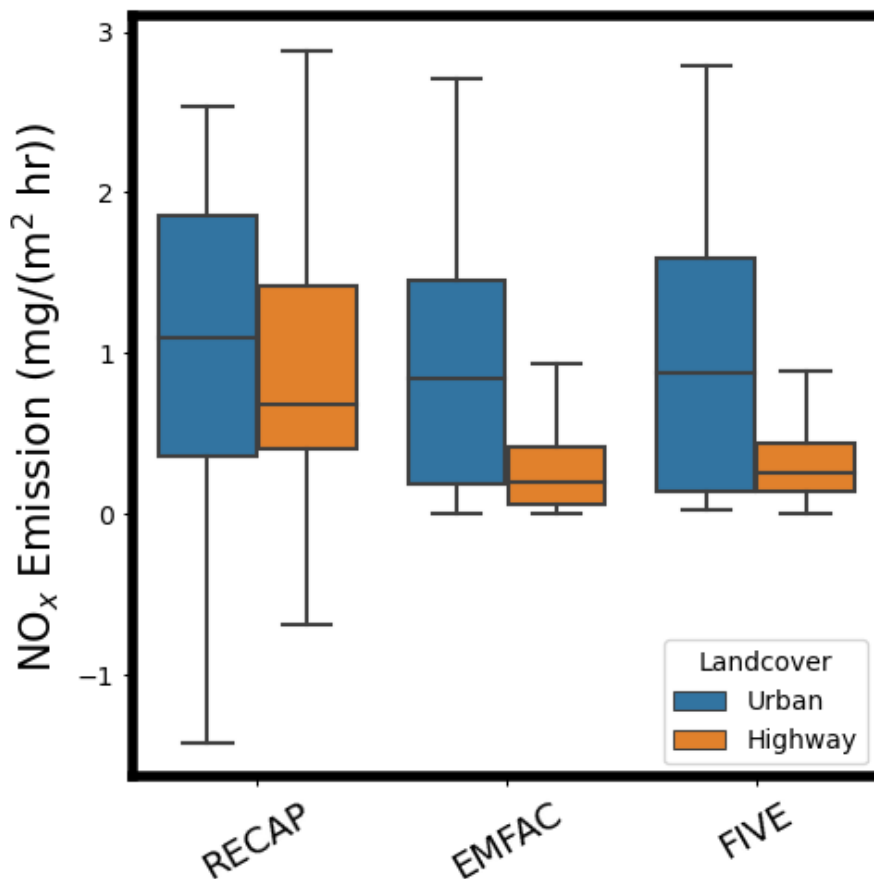
Figure 6. Whisker box plot of observed RECAP anthropogenic NO_x emissions from transportation and fuel combustion as well as those from EMFAC and FIVE emission inventories, separated by highway and urban land cover types. The box is the interquartile range with the line of the median value. The maximum and minimum emissions are shown by whiskers.

both have an order of magnitude lower emissions with median soil NO_x emissions of 0.018, 0.023 mg m^{-2} h^{-1}, respectively. The BDISNP soil NO_x scheme shows a median soil NO_x emission of 0.32 mg m^{-2} h^{-1}. Figure. 7 (b) exhibits a point-by-point comparison of the observed RECAP and the BDISNP soil NO_x emissions showing that there is a correspondence between the two but the model is 2.7 times lower than the observations. Figure S9 (a) and (d) shows the spatial distribution of soil NO_x emissions from observation and BDISNP scheme. Both show higher soil NO_x emissions between 35.75 °N and 36.25 °N.

A distinct characteristic of soil NO_x emission is its temperature dependence. For instance, Oikawa et al. (2015) identified unusually high soil NO_x emissions in a high-temperature agricultural region based on in-situ observations. The temperature-driven increase in soil NO_x emission raises concerns in the future warmer climate, resulting in a larger contribution to O_3 pollution (Romer et al., 2018). Here we leverage our flux observations to probe this temperature dependence. We collect observed NO_x emissions for each flight and select the subset of NO_x emissions on grids categorized as cultivated soil land
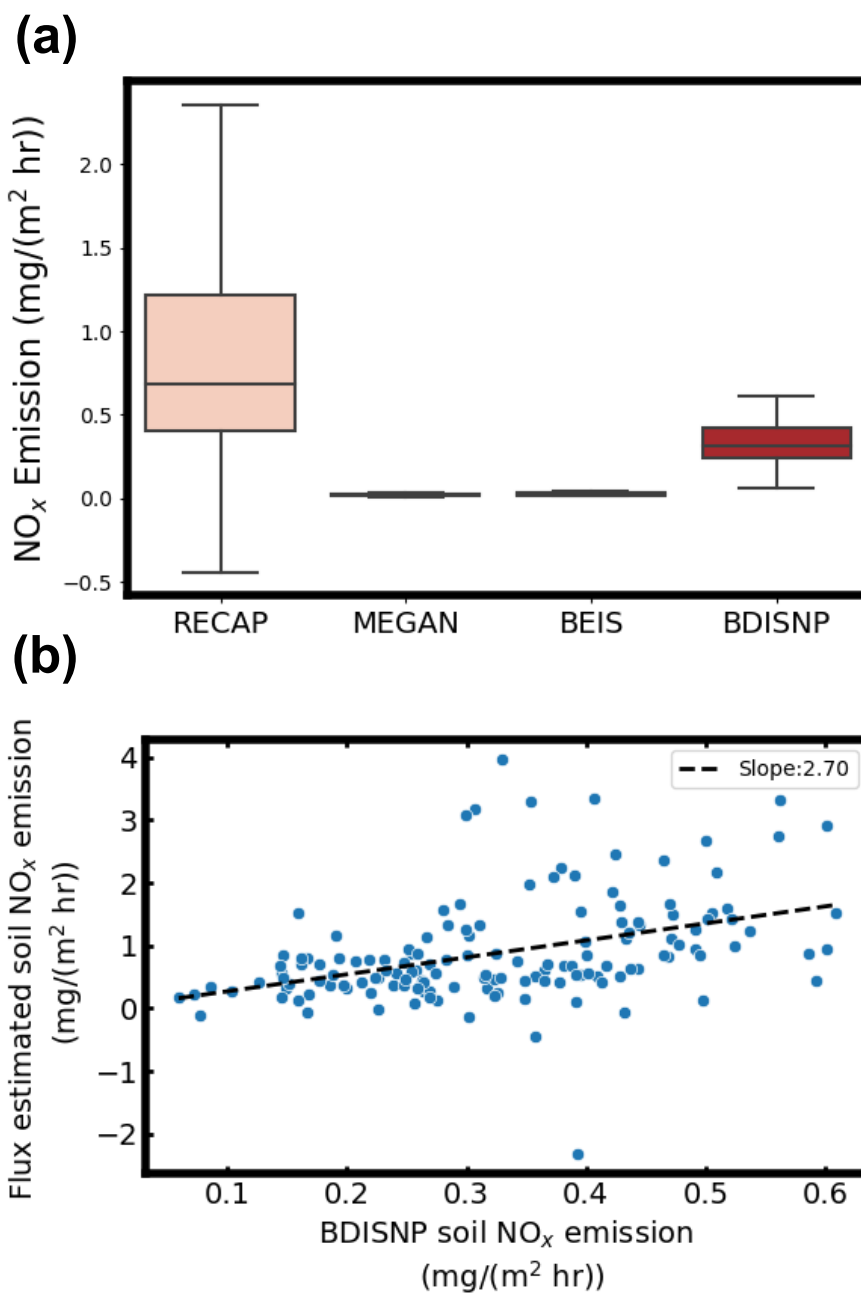
Figure 7. a) The whisker box plot of observed soil NO_x emissions and parameterized soil NO_x emissions from MEGAN, BEIS and BDISNP schemes. b) The scatter plot of soil NO_x emissions calculated from BDISNP scheme and from flux measurements. The dashed black is the least-square linear fit.
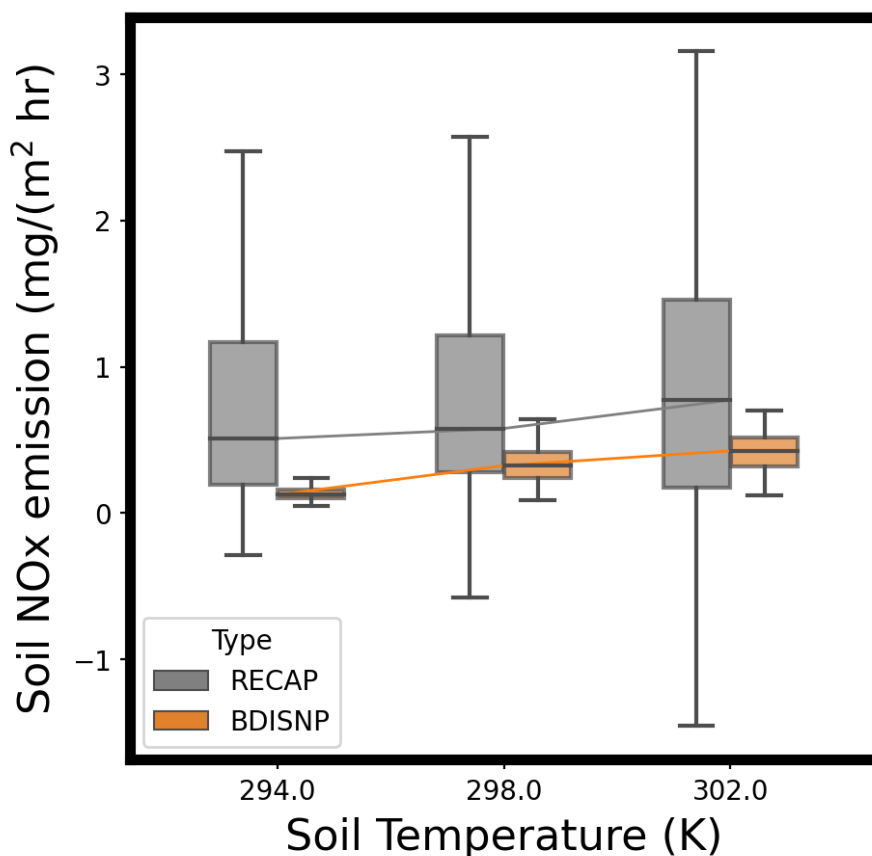
Figure 8. The dependence of soil NO_x emissions on soil temperature from both flux measurements (gray) and BDISNP scheme (orange). Both observed and BDISNP soil NO_x emissions are binned based on mean soil temperature from WRF-Chem. Three soil temperature bins are described with 4k intervals. The whisker box shows the distribution within each bin and the line connects median soil NO_x emissions across three bins.

type. We also collect corresponding mean soil temperature from WRF-Chem and match them to observed NO_x emissions both

300 in time and space. A large variation of soil temperature is observed, ranging from 292K to 304K. We then bin observed soil NO_x emissions to three soil temperature categories, each of which has 4K intervals. The median soil NO_x emissions increase from 0.51 mg m^{-2} h^{-1} to 0.77 mg m^{-2} h^{-1} with the mean soil temperature increasing from 294 K to 302 K. As the response to soil temperature is incorporated in the BDISNP scheme, we also bin the BDISNP parameterized soil NO_x emissions into the same soil temperature categories. Both the RECAP measured flux and the BDISNP modeled soil NO_x emissions exhibit

305 an approximately 33% increase over the range of soil temperature shown.

6 Conclusions

We performed airborne NO_x flux measurements during RECAP-CA field campaign over the San Joaquin Valley. Seven flights were made over the SJV in June 2021. When combined with footprint and land cover information, we resolve spatial heterogeneity in landscape flux. The component fluxes are estimated based on the multi-linear regression and exhibit statistically significant differences. The component fluxes are the highest from highways at 2.95 mg m^{-2} h^{-1}. Cultivated soil land types emit a non-negligible flux of 0.79 mg m^{-2} h^{-1}. The airborne flux observations are projected to a 4 km grid spacing to yield an estimated emission map over the SJV. We utilize this map to evaluate emission inventories commonly used in photochemical modeling. The anthropogenic emission inventories, EMFAC and FIVE, agree with estimated NO_x emissions over urban regions within 27% and 24%, respectively. However, the widely used, but not state-of-the-science, models for soil NO_x emissions underestimate emissions by an order of magnitude or more in the SJV, leading to a poor assessment of the relative roles of mobile and agriculture sources of NO_x in the region. The BDISNP model as adapted by Sha et al. (2021) results in a better comparison with the observations. Even though it is still lower by a factor of 2.7, we show it yields a similar spatial pattern and soil temperature dependence as observed. Variations of this model are embedded in CMAQ (Rasool et al., 2019) and GEOS-CHEM (Wang et al., 2021) and have been implemented in WRF-CHEM by(Sha et al., 2021). Studies, where soil NO_x is potentially important, should make use of these codes, all of which are more consistent with observations at multiple scales.

Code and data availability. The measurement data from the RECAP field champaign is available at https://csl.noaa.gov/projects/sunvex/. The analysis codes for this study are available at https://github.com/qdzhu/FLUX/.

Author contributions. RCC and AHG supervised the research; BP, EP, BS, PW CA, AB, JS, RCC, AHG participated in the field campaign; BP and PW conducted the NO_x measurements; ST, HZ and JW provided model simulated BDISNP soil NO_x emissions; QZ performed the analysis with contributions from BP, EP, CN; QZ prepared the manuscript; all authors have reviewed and edited the paper.

Competing interests. The authors have the following competing interests: At least one of the (co-)authors is a member of the editorial board of Atmospheric Chemistry and Physics.

Acknowledgements. This RECAP field campaign was funded by California Air Resources Board Contract number 20RD003, 20AQP012, and Presidential Early Career Award for Scientists and Engineers (PECASE) (from Brian McDonald). QZ was supported by NOAA Climate & Global Change Postdoc Fellowship and EP was supported by a Feodor Lynen Fellowship of the Alexander von Humboldt Foundation. We thank Dennis Baldocchi, Glenn Wolfe, Erin Delaria for their help in calculating vertical divergence, and Brian McDonald, Rebecca Schwantes, Siyuan Wang for engaging in discussions at project meetings. We appreciate use of the emission inventories provided by Modeling

and Meteorology Branch at CARB and NOAA Chemical Sciences Laboratory. We acknowledge the help from pilots, Bryce Kujat and George Loudakis, during the RECAP field campaign.

References

Almaraz, M., Bai, E., Wang, C., Trousdell, J., Conley, S., Faloona, I., and Houlton, B. Z.: Agriculture is a major source of NO x pollution in California, Science advances, 4, eaao3477, 2018.

American Lung Association: State of the Air Report, https://www.lung.org/research/sota, last accessed on 06/22/2022, 2020.

Andreae, M. O. and Schimel, D. S.: Exchange of trace gases between terrestrial ecosystems and the atmosphere, 1990.

CARB: Heavy-Duty Engine and Vehicle Omnibus Regulation and Associated Amendments, https://ww2.arb.ca.gov/rulemaking/2020/hdomnibuslownox, last accessed on 06/22/2022, 2016.

CARB: EMission FACtor (EMFAC), https://arb.ca.gov/emfac/, last accessed on 06/22/2022, 2021a.

CARB: OFFROAD2021 model, https://ww2.arb.ca.gov/our-work/programs/mobile-source-emissions-inventory/msei-road-documentation-0, last accessed on 06/22/2022, 2021b.

CARB: Stationary Emissions by Air District, https://ww2.arb.ca.gov/applications/emissions-air-district, last accessed on 06/22/2022, 2021c.

Day, D., Wooldridge, P., Dillon, M., Thornton, J., and Cohen, R.: A thermal dissociation laser-induced fluorescence instrument for in situ detection of NO2, peroxy nitrates, alkyl nitrates, and HNO3, Journal of Geophysical Research: Atmospheres, 107, ACH–4, 2002.

De Gouw, J. A., Parrish, D. D., Frost, G. J., and Trainer, M.: Reduced emissions of CO2, NOx, and SO2 from US power plants owing to switch from coal to natural gas with combined cycle technology, Earth's Future, 2, 75–82, 2014.

Drysdale, W. S., Vaughan, A. R., Squires, F. A., Cliff, S. J., Metzger, S., Durden, D., Pingintha-Durden, N., Helfter, C., Nemitz, E., Grimmond, C. S. B., et al.: Eddy Covariance Measurements Highlight Sources of Nitrogen Oxide Emissions Missing from Inventories for Central London, Atmospheric Chemistry and Physics Discussions, pp. 1–35, 2022.

EPA: Air Pollutant Emissions Trends Data, https://www.epa.gov/air-emissions-inventories/air-pollutant-emissions-trends-data, last accessed on 10/28/2021, 2016.

Gu, D., Guenther, A. B., Shilling, J. E., Yu, H., Huang, M., Zhao, C., Yang, Q., Martin, S. T., Artaxo, P., Kim, S., et al.: Airborne observations reveal elevational gradient in tropical forest isoprene emissions, Nature communications, 8, 1–7, 2017.

Guenther, A., Jiang, X., Heald, C. L., Sakulyanontvittaya, T., Duhl, T. a., Emmons, L., and Wang, X.: The Model of Emissions of Gases and Aerosols from Nature version 2.1 (MEGAN2. 1): an extended and updated framework for modeling biogenic emissions, Geoscientific Model Development, 5, 1471–1492, 2012.

Guo, L., Chen, J., Luo, D., Liu, S., Lee, H. J., Motallebi, N., Fong, A., Deng, J., Rasool, Q. Z., Avise, J. C., et al.: Assessment of nitrogen oxide emissions and San Joaquin Valley PM2. 5 impacts from soils in California, Journal of Geophysical Research: Atmospheres, 125, e2020JD033 304, 2020.

Hakeem, K. R., Sabir, M., Ozturk, M., Akhtar, M., Ibrahim, F. H., et al.: Nitrate and nitrogen oxides: sources, health effects and their remediation, Reviews of Environmental Contamination and Toxicology Volume 242, pp. 183–217, 2016.

Hannun, R. A., Wolfe, G. M., Kawa, S. R., Hanisco, T. F., Newman, P. A., Alfieri, J. G., Barrick, J., Clark, K. L., DiGangi, J. P., Diskin, G. S., et al.: Spatial heterogeneity in CO2, CH4, and energy fluxes: Insights from airborne eddy covariance measurements over the Mid-Atlantic region, Environmental Research Letters, 15, 035 008, 2020.

Harkins, C., McDonald, B. C., Henze, D. K., and Wiedinmyer, C.: A fuel-based method for updating mobile source emissions during the COVID-19 pandemic, Environmental Research Letters, 16, 065 018, 2021.

Högström, U.: Non-dimensional wind and temperature profiles in the atmospheric surface layer: A re-evaluation, in: Topics in Micrometeorology. A Festschrift for Arch Dyer, pp. 55–78, Springer, 1988.

Hudman, R., Moore, N., Mebust, A., Martin, R., Russell, A., Valin, L., and Cohen, R.: Steps towards a mechanistic model of global soil nitric oxide emissions: implementation and space based-constraints, Atmospheric Chemistry and Physics, 12, 7779–7795, 2012.

Hutjes, R., Vellinga, O., Gioli, B., and Miglietta, F.: Dis-aggregation of airborne flux measurements using footprint analysis, Agricultural
375 and Forest Meteorology, 150, 966–983, 2010.

Kampa, M. and Castanas, E.: Human health effects of air pollution, Environmental pollution, 151, 362–367, 2008.

Karl, T., Apel, E., Hodzic, A., Riemer, D., Blake, D., and Wiedinmyer, C.: Emissions of volatile organic compounds inferred from airborne flux measurements over a megacity, Atmospheric Chemistry and Physics, 9, 271–285, 2009.

Karl, T., Misztal, P., Jonsson, H., Shertz, S., Goldstein, A., and Guenther, A.: Airborne flux measurements of BVOCs above Californian oak
380 forests: Experimental investigation of surface and entrainment fluxes, OH densities, and Damköhler numbers, Journal of the atmospheric sciences, 70, 3277–3287, 2013.

Kaser, L., Karl, T., Yuan, B., Mauldin III, R., Cantrell, C., Guenther, A. B., Patton, E., Weinheimer, A. J., Knote, C., Orlando, J., et al.: Chemistry-turbulence interactions and mesoscale variability influence the cleansing efficiency of the atmosphere, Geophysical Research Letters, 42, 10–894, 2015.

385 Kim, S.-W., McDonald, B. C., Seo, S., Kim, K.-M., and Trainer, M.: Understanding the paths of surface ozone abatement in the Los Angeles Basin, Journal of Geophysical Research: Atmospheres, 127, e2021JD035 606, 2022.

Kljun, N., Calanca, P., Rotach, M., and Schmid, H.: A simple parameterisation for flux footprint predictions, Boundary-Layer Meteorology, 112, 503–523, 2004.

Lelieveld, J., Evans, J. S., Fnais, M., Giannadaki, D., and Pozzer, A.: The contribution of outdoor air pollution sources to premature mortality
390 on a global scale, Nature, 525, 367–371, 2015.

Lenschow, D., Mann, J., and Kristensen, L.: How long is long enough when measuring fluxes and other turbulence statistics?, Journal of Atmospheric and Oceanic Technology, 11, 661–673, 1994.

Mauder, M., Desjardins, R. L., and MacPherson, I.: Scale analysis of airborne flux measurements over heterogeneous terrain in a boreal ecosystem, Journal of Geophysical Research: Atmospheres, 112, 2007.

395 McDonald, B. C., Dallmann, T. R., Martin, E. W., and Harley, R. A.: Long-term trends in nitrogen oxide emissions from motor vehicles at national, state, and air basin scales, Journal of Geophysical Research: Atmospheres, 117, 2012.

Metzger, S., Junkermann, W., Mauder, M., Beyrich, F., Butterbach-Bahl, K., Schmid, H.-P., and Foken, T.: Eddy-covariance flux measurements with a weight-shift microlight aircraft, Atmospheric Measurement Techniques, 5, 1699–1717, 2012.

Misztal, P., Karl, T., Weber, R., Jonsson, H., Guenther, A. B., and Goldstein, A. H.: Airborne flux measurements of biogenic isoprene over
400 California, Atmospheric Chemistry and Physics, 14, 10 631–10 647, 2014.

Oikawa, P., Ge, C., Wang, J., Eberwein, J., Liang, L., Allsman, L., Grantz, D., and Jenerette, G.: Unusually high soil nitrogen oxide emissions influence air quality in a high-temperature agricultural region, Nature communications, 6, 1–10, 2015.

Phoenix, G. K., Hicks, W. K., Cinderby, S., Kuylenstierna, J. C., Stock, W. D., Dentener, F. J., Giller, K. E., Austin, A. T., Lefroy, R. D., Gimeno, B. S., et al.: Atmospheric nitrogen deposition in world biodiversity hotspots: the need for a greater global perspective in assessing
405 N deposition impacts, Global Change Biology, 12, 470–476, 2006.

Rasool, Q. Z., Bash, J. O., and Cohan, D. S.: Mechanistic representation of soil nitrogen emissions in the Community Multiscale Air Quality (CMAQ) model v 5.1, Geoscientific Model Development, 12, 849–878, 2019.

Romer, P. S., Duffey, K. C., Wooldridge, P. J., Edgerton, E., Baumann, K., Feiner, P. A., Miller, D. O., Brune, W. H., Koss, A. R., De Gouw, J. A., et al.: Effects of temperature-dependent NO x emissions on continental ozone production, Atmospheric Chemistry and Physics, 18, 2601–2614, 2018.

Sayres, D. S., Dobosy, R., Healy, C., Dumas, E., Kochendorfer, J., Munster, J., Wilkerson, J., Baker, B., and Anderson, J. G.: Arctic regional methane fluxes by ecotope as derived using eddy covariance from a low-flying aircraft, Atmospheric Chemistry and Physics, 17, 8619–8633, 2017.

Schaller, C., Göckede, M., and Foken, T.: Flux calculation of short turbulent events–comparison of three methods, Atmospheric Measurement Techniques, 10, 869–880, 2017.

Sha, T., Ma, X., Zhang, H., Janechek, N., Wang, Y., Wang, Y., Castro Garci´a, L., Jenerette, G. D., and Wang, J.: Impacts of Soil NO x Emission on O3 Air Quality in Rural California, Environmental science & technology, 55, 7113–7122, 2021.

Sühring, M., Metzger, S., Xu, K., Durden, D., and Desai, A.: Trade-offs in flux disaggregation: a large-eddy simulation study, Boundary-Layer Meteorology, 170, 69–93, 2019.

Thornton, J. A., Wooldridge, P. J., and Cohen, R. C.: Atmospheric NO2: In situ laser-induced fluorescence detection at parts per trillion mixing ratios, Analytical Chemistry, 72, 528–539, 2000.

Vaughan, A. R., Lee, J. D., Misztal, P. K., Metzger, S., Shaw, M. D., Lewis, A. C., Purvis, R. M., Carslaw, D. C., Goldstein, A. H., Hewitt, C. N., et al.: Spatially resolved flux measurements of NO x from London suggest significantly higher emissions than predicted by inventories, Faraday discussions, 189, 455–472, 2016.

Vaughan, A. R., Lee, J. D., Metzger, S., Durden, D., Lewis, A. C., Shaw, M. D., Drysdale, W. S., Purvis, R. M., Davison, B., and Hewitt, C. N.: Spatially and temporally resolved measurements of NO x fluxes by airborne eddy covariance over Greater London, Atmospheric Chemistry and Physics, 21, 15 283–15 298, 2021.

Wang, Y., Ge, C., Garcia, L. C., Jenerette, G. D., Oikawa, P. Y., and Wang, J.: Improved modelling of soil NO x emissions in a high temperature agricultural region: role of background emissions on NO2 trend over the US, Environmental research letters, 16, 084 061, 2021.

Wolfe, G., Hanisco, T., Arkinson, H., Bui, T., Crounse, J., Dean-Day, J., Goldstein, A., Guenther, A., Hall, S., Huey, G., et al.: Quantifying sources and sinks of reactive gases in the lower atmosphere using airborne flux observations, Geophysical Research Letters, 42, 8231–8240, 2015.

Wolfe, G. M., Kawa, S. R., Hanisco, T. F., Hannun, R. A., Newman, P. A., Swanson, A., Bailey, S., Barrick, J., Thornhill, K. L., Diskin, G., et al.: The NASA carbon airborne flux experiment (CARAFE): instrumentation and methodology, Atmospheric Measurement Techniques, 11, 1757–1776, 2018.

Wooldridge, P., Perring, A., Bertram, T., Flocke, F., Roberts, J., Singh, H., Huey, L., Thornton, J., Wolfe, G., Murphy, J., et al.: Total Peroxy Nitrates (ΣPNs) in the atmosphere: the Thermal Dissociation-Laser Induced Fluorescence (TD-LIF) technique and comparisons to speciated PAN measurements, Atmospheric Measurement Techniques, 3, 593–607, 2010.

Yu, H., Guenther, A., Gu, D., Warneke, C., Geron, C., Goldstein, A., Graus, M., Karl, T., Kaser, L., Misztal, P., et al.: Airborne measurements of isoprene and monoterpene emissions from southeastern US forests, Science of the Total Environment, 595, 149–158, 2017.

Yuan, B., Kaser, L., Karl, T., Graus, M., Peischl, J., Campos, T. L., Shertz, S., Apel, E. C., Hornbrook, R. S., Hills, A., et al.: Airborne flux measurements of methane and volatile organic compounds over the Haynesville and Marcellus shale gas production regions, Journal of Geophysical Research: Atmospheres, 120, 6271–6289, 2015.